DIRECT NUMERICAL SIMULATION OF SECONDARY CURRENTS IN ARTERIAL FLOWS WITH STENTS

Jonathan Neuhauser, Niklas Langer, Alexander Stroh
Institute of Fluid Mechanics
Karlsruhe Institute of Technology
Kaiserstr. 10, 76131 Karlsruhe, Germany
alexander.stroh@kit.edu

Andrea Zampiron
Department of Civil, Environmental and Architectural Engineering
University of Padua
Via 8 Febbraio 2, 35122 Padova, Italy
andrea.zampiron@unipd.it

ABSTRACT

Direct numerical simulations are performed to investigate secondary motions induced by stent-like geometries in laminar and turbulent pipe flow. Three configurations of increasing complexity are considered: straight ridges, helical ridges, and ambihelical ridges. In laminar flow, only weak modifications of the mean velocity are observed, with secondary currents arising mainly from pressure gradients. In contrast, turbulent flow produces strong secondary motions: counter-rotating vortices for straight ridges, and large-scale cross-sectional rotation for the helical case. The skin friction coefficient increases with geometric complexity, with helical ridges yielding the strongest enhancement due to combined pressure-driven and turbulence-induced mechanisms. These results highlight the significant role of stent structures in shaping secondary currents and transport processes.

ARTERIAL FLOW WITH STENTS

Between 30% and 40% of deaths from cardiovascular disease are due to atherosclerosis (Timmis et al. 2024), a condition characterized by the build-up of plaque (deposits of fatty substances, cholesterol, and other materials) in the coronaries. The resulting narrowing of these arteries, known as stenosis, reduces blood flow to the myocardium and, in severe cases, may lead to heart attacks. Stenosis is often treated with angioplasty (a surgical procedure that expands the artery to approximately its original diameter) followed by the implantation of a stent, a tubular mesh that helps maintain the restored artery configuration over time.

The thickness of stents is $\Delta \approx 0.1-0.2$ mm for metallic stents and $\Delta \approx 0.3-0.5$ mm for stent grafts. Stents are typically designed to maximize mechanical performance (e.g., preventing rupture), while their effects on arterial hemodynamics are often underestimated, likely due to their small relative thickness Δ/D (D is artery diameter, i.e., $D \approx 3-5$ mm for the coronaries and $D \approx 15-30$ mm for the aorta). This is particularly true when considering flow disturbances at the scale of D. However, wall roughness with $\Delta/\delta \ll 1$ (δ is flow outer scale) has been shown to generate large-scale time-averaged streamwise rotational motions (Vanderwel and Ganapathisubramani 2015), known as secondary currents (SCs), which are expected to affect wall shear stress, flow drag, pressure losses, momentum and energy exchange, and the transport of particles and substances, among other effects.

According to Prandtl, SCs can be divided into two categories: (i) SCs of the first kind, generated by spatial gradients of time-averaged velocities (often referred to as pressure-driven), which may occur in both laminar and turbulent flow regimes; and (ii) SCs of the second type, generated by turbulence anisotropy. Arterial flows are characterized by laminar to mildly turbulent conditions, where both types of SCs can emerge, compete, and interact. The aim of this work is therefore to study roughness-induced SCs in arterial flow, with particular attention to the role of turbulence relative to mean velocity gradients.

METHODOLOGY

Three different stent-like geometries are considered as shown in fig. 1(a). The reference domain is a circular pipe with semicircular ridge cut-outs of diameter $\Delta = 0.1D$, where D is the pipe diameter. S1 contains four ridges extruded in the streamwise direction. In S2 the ridges undergo a rotation in positive φ-direction along the z-axis, forming a left-handed helix with inclination angle $\gamma = \pi/4$. S3 combines this with an additional right-handed helix, resulting in eight ridges and intersections not present in S1 or S2.

The DNS are carried out with the spectral element solver NekRS v23.0 (Fischer et al. 2022) using BDF2/EXT2 time stepping and polynomial order $N = 7$ with Gauss–Lobatto–Legendre quadrature points. No-slip boundary conditions are applied at the walls, periodic conditions in z, and the flow is driven by a constant pressure gradient. Laminar and turbulent regimes are represented by $Re_\tau = 60$ and 180, respectively. Domain lengths are chosen as $L_z = \pi D$ for laminar S2 and S3, $L_z = 0.1D$ for laminar S1, and $L_z = 4\pi D$ for all turbulent cases. The mesh resolution is adjusted to satisfy $\Delta r^+ \leq 1$ at the wall, where r is the radial axis and superscripted "+" represents viscous scaling. For the turbulent cases the flow field is temporally averaged for a sufficient period of simulation time after a fully developed

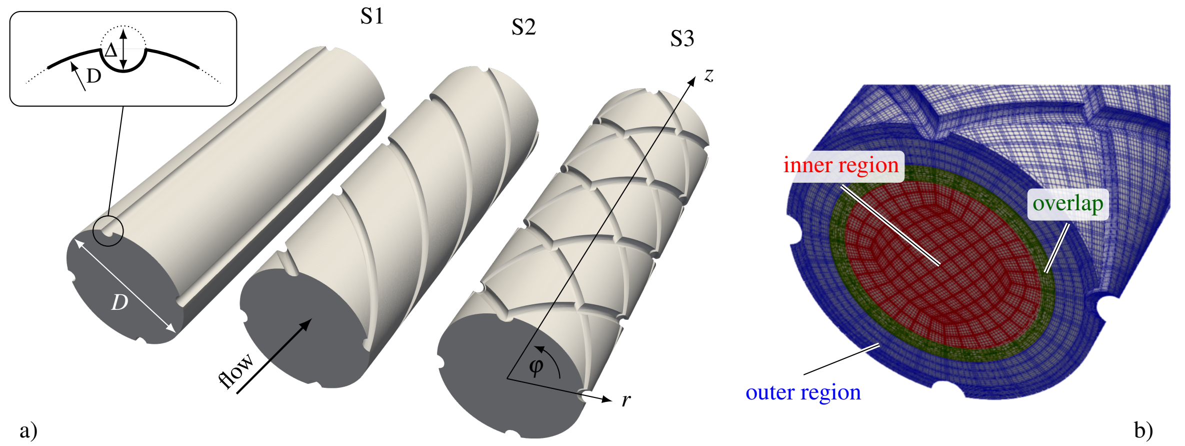

Figure 1. Three considered stent geometries: S1 - straight ridges, S2 - helical ridges, S3 - ambihelical ridges (a) with exemplarily overset mesh topology for the case S3 (b).

state is achieved.

To ensure flexibility in mesh generation, the overset *neknek* approach is employed (Mittal et al. 2019). As shown in fig. 1(b), the computational domain is split into an inner cylindrical region, identical for all cases, and an outer region fitted to the respective geometry: simple extrusion for S1, rotation for S2, and combined fitting for S3.

RESULTS

Skin Friction Coefficient

	Re_τ	S0	S1	S2	S3
D_h/D		1.000	0.920	0.892	0.823
$C_f \cdot 10^2$	60	0.889	0.908	1.064	1.225
	180	0.925	0.873	1.703	3.022
Re_b	60	1800	1571	1386	1145
	180	5294	4807	3286	2186
$\Omega_z D_h^2/U_b^2$	60	0.000	0.000	0.844	1.105
	180	0.000	0.111	10.274	14.491

Table 1. Hydraulic diameter, skin friction coefficient, bulk Reynolds number and dimensionless specific enstrophy for the considered cases.

Table 1 summarizes the hydraulic diameter $D_h = 4V/S$, the skin friction coefficient $C_f = 2\tau_w/\rho U_b^2$ with $\tau_w = -(D_h/4)\,\mathrm{d}p/\mathrm{d}x$, the bulk Reynolds number $\mathrm{Re}_b = U_b D_h/\nu$, and the normalized specific enstrophy $\Omega_z = 1/V \int \omega_z^2 \,\mathrm{d}V$ for the considered cases. For the straight-ridge configuration S1 in the laminar regime, the C_f is increased by around 2% compared to the smooth-pipe counterpart, while in the turbulent regime, the C_f is reduced by $\sim 5\%$. Introducing the helical structure S2 leads to a 20% and 84% increase in C_f for the laminar and turbulent cases, respectively. In the turbulent regime, this stronger rise in C_f is accompanied by a substantial enhancement of rotational energy, with Ω_z reaching values about one hundred times higher than those of the straight-ridge case. For the ambihelical geometry S3, C_f increases by 38% and 225% for the laminar and turbulent regimes, respectively, while Ω_z also shows a significant increase compared to S2.

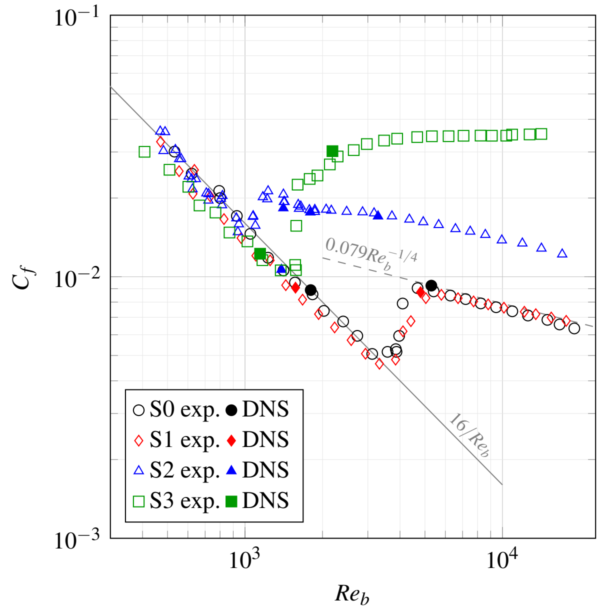

Figure 2. Comparison of the skin friction coefficient with experimental results (Proceeding ID501 by Zampiron et al.).

This might indicate that the additional drag is related not only to the larger wetted surface area of the structure (8 ridges for S3 vs. 4 ridges for S2), but also to enhanced rotational motions present for this particular case. However, one has to note that comparisons of C_f between different geometries are strongly biased by the choice of the reference height for each geometry – here the hydraulic diameter D_h – and that the pressure gradient (Re_τ) is fixed between geometries, not the flow rate (Re_b).

Figure 2 compares the numerical results with the experimental study, where the resultant C_f was determined through pressure drop measurements across a range of Re_b in both laminar and turbulent flow regimes. For extensive details on the experimental methodology, the reader is referred to the work by Zampiron et al. (proceeding ID501). The experimental data for the smooth pipe (S0) align closely with the analytical laminar solution $C_f = 16/\mathrm{Re}_b$ and the turbulent Blasius correlation $C_f = 0.079\,\mathrm{Re}_b^{-0.25}$, with a transition region observed between $\mathrm{Re}_b = 3000$ and 5000. The straight-ridge geometry

S1 closely follows the C_f curve of the smooth pipe, showing slightly lower values in the laminar regime while remaining nearly indistinguishable from S0 in the turbulent regime. Both helical and ambihelical geometries demonstrate markedly different trends. While the C_f of the helical-ridge geometry S2 follows the analytical laminar solution with a slight downward shift for $\mathrm{Re}_b < 1000$ before transitioning, its turbulent distribution maintains the same slope as the S0 and S1 cases but is shifted to significantly higher values. For the ambihelical configuration S3, even lower C_f values are observed in the laminar regime, with transition occurring at $\mathrm{Re}_b \approx 1500$. At higher Re_b, the C_f for S3 saturates and exhibits a nearly constant value. This behavior resembles the well-known fully-rough regime for rough surfaces, where at higher Reynolds numbers frictional drag becomes independent of viscous effects and form drag becomes dominant. Overall, seven of the eight numerically predicted C_f values demonstrate excellent agreement with the experimental measurements. The only notable deviation occurs for the helical geometry S2 at $\mathrm{Re}_\tau = 60$. This discrepancy is attributed to the early transition to turbulence observed in the experiment at $\mathrm{Re}_b \approx 1000$. In contrast, the numerical domain for this specific case was explicitly configured with a streamwise length ($L_z = \pi D$) designed to accommodate and maintain a fully developed laminar state. Consequently, the DNS result aligns with the laminar analytical solution rather than capturing the elevated C_f values associated with the experimental transitional regime. To further investigate this behaviour, supplementary simulations were conducted in a longer domain using a turbulent snapshot as initial condition at $Re_\tau = 80$ and 100 (see two additional points for S2 in Fig. 2). The obtained values align well with the experimental data. In contrast, the simulation at $Re_\tau = 60$ was initialised with a laminar smooth-wall velocity profile. It is known that transition to turbulence is rather sensitive on initial conditions (Faisst and Eckhardt 2004). However, both numerical and experimental data show that the presence of (ambi)helical ridges significantly reduces the value of Re_b at which turbulence can be sustained. This can be attributed to the streamwise vorticity introduced by the azimuthal deflection at the ridges.

Consistent with the experimental observations, the numerical results exhibit lower C_f values for the structured geometries compared to the smooth-pipe baseline in the laminar regime. This trend is primarily attributed to the definition of the hydraulic diameter D_h, which exerts a dominant influence on the skin friction coefficient in the laminar regime ($C_f \propto D_h^3$ when considering the sensitivity of pressure drop to the characteristic length scale). Conversely, in the turbulent regime, the drag behavior is governed by the significant deformation of the mean velocity profile and the emergence of intense secondary currents, which enhance momentum transport regardless of the geometric scaling.

Mean Velocity Distribution

The resulting mean velocity profiles with the associated SC topology for the considered geometries are shown in fig. 3. For visualization, spatial averaging was applied in the streamwise direction for the straight ridges (S1) and along the helical path for the helical ridges (S2). The complex three-dimensional flow of the cross-helical geometry (S3) is shown without spatial averaging at a single slice $z = 0$. The intensity of the SCs is quantified in fig. 3 (right half of each panel) using their cross-sectional magnitude. In the laminar regime, the presence of ridges has only a minor influence on the mean velocity distribution. For geometries S1 and S2, the deformation is weak and confined to the vicinity of the ridges, whereas in S3 the bulging of the velocity profile is more pronounced. This behavior is directly linked to the topology of the SCs. In S1, no SCs are observed, and consequently no radial velocities appear that could modify the mean velocity field. In contrast, the helical structure of S2 induces mean axial rotation onto the flow, guided by the direction of the ridges. The cross-stream component is mainly in the azimuthal direction, and reaches up to 10% of U_b near the wall. Since the radial velocity component remains small, the mean velocity profile itself shows little deformation. As the solution is steady and laminar, the in-plane components are driven by pressure, i.e. are SCs of Prandtl's first kind. For S3, SCs form locally near the ridges with magnitudes up to 5% of U_b at $z = 0$. These motions originate from the deflection of the streamwise velocity caused by the ambihelical ridge arrangement and can likewise be classified as SCs of Prandtl's first kind.

In the turbulent regime, the mean streamwise velocity distributions exhibit much steeper velocity gradients at the walls and more homogeneous, flattened profiles in the bulk of the flow. For geometry S1, large-scale SCs develop, characterized by two counter-rotating vortices above each ridge. The associated wall-normal uplift towards the pipe centerline reaches up to 4-5% of U_b, producing a pronounced deformation of the mean velocity distribution with low-speed regions protruding into the bulk flow. This case represents a classical example of SC of Prandtl's second kind, where the anisotropy of turbulence, induced by wall inhomogeneities, drives the secondary flow. For the helical configuration S2, a very strong in-plane rotational motion is observed, with magnitudes reaching up to 32% of U_b. The stronger impact of ridges in the turbulent regime is attributed to the higher impingement velocities on the structures, resulting from the steeper near-wall velocity gradients characteristic of turbulence. The topology is similar to that of the laminar case; however, in this regime the SC is likely sustained by a combination of pressure gradients and turbulence anisotropy. In S3, the turbulent flow again produces a SC pattern resembling that of the laminar case, but with a much greater strength, reaching up to 18% of U_b. For S3 it should be noted that the modification of the mean velocity profile and the associated SC are highly three-dimensional, exhibiting recirculation zones (marked in purple in Fig. 3).

Decomposition of Bulk Mean Velocity

Double integration of the streamwise mean momentum equation delivers a decomposition of the bulk mean velocity similar to the one introduced by Marusic et al. (2007) or Benschop and Breugem (2017). For a cylindrical pipe flow, the following contribution terms can be identified:

$$U_b = \frac{2}{R^2} \int_0^R \langle \bar{u}_z \rangle \, r \, \mathrm{d}r = U_b^L + U_b^R + U_b^{RS} + U_b^{DS} + U_b^D. \quad (1)$$

U_b^L represents the laminar contribution for a pipe:

$$U_b^L = \frac{\mathrm{Re}_\tau}{4}. \quad (2)$$

U_b^R is the contribution related to the reduction of the effective pipe radius due to the structuring, where $R_{\mathrm{eff}} = \sqrt{V/\pi L_z}$:

$$U_b^R = \frac{\mathrm{Re}_\tau}{4} \left(\frac{R_{\mathrm{eff}}}{1 - R_{\mathrm{eff}}} \right). \quad (3)$$

U_b^{RS} and U_b^{DS} are the drag penalties related to the turbulent random Reynolds shear stresses $\langle \overline{u_r'' u_z''} \rangle$ and the dispersive

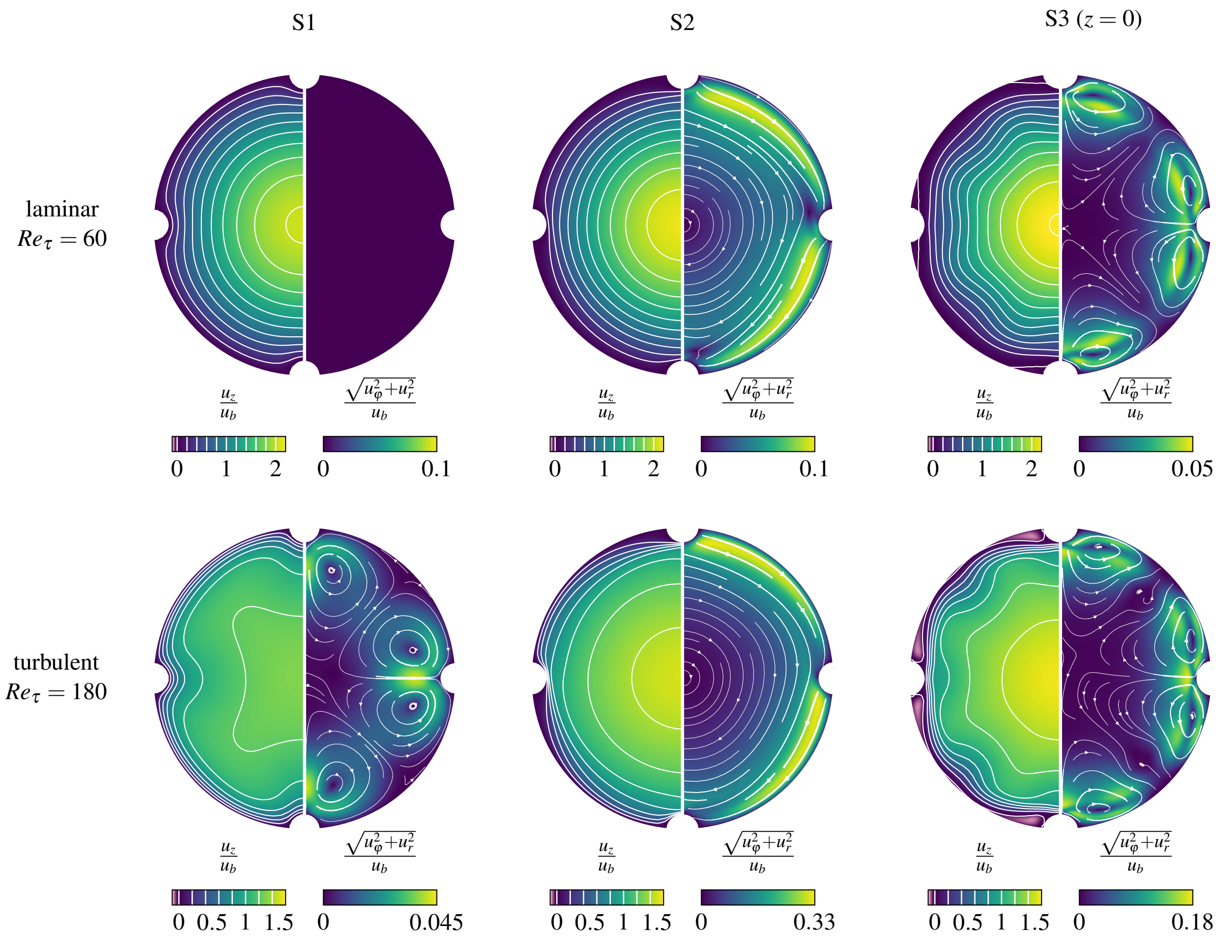

Figure 3. Streamwise mean velocity profiles (left half of each panel, contours and background) and secondary-current topology (right half of each panel, background: magnitude of the in-plane velocity) for the considered geometrical configurations in the laminar and turbulent flow regime. While spatial averaging is applied in z-direction and along the helical structure for S1 and S2, respectively, for S3 the cross-sectional slice at $z = 0$ is shown.

stresses $\langle \tilde{u}_r \tilde{u}_z \rangle$, which are often directly linked to the presence of SC:

$$U_b^{RS} = -\int_0^R \left(\frac{r}{R}\right)^2 \langle \overline{u_r'' u_z''} \rangle^+ \, \mathrm{d}r, \tag{4}$$

$$U_b^{DS} = -\int_0^R \left(\frac{r}{R}\right)^2 \langle \tilde{u}_r \tilde{u}_z \rangle^+ \, \mathrm{d}r. \tag{5}$$

The last term, U_b^D, represents the contribution of the structural geometry to the overall drag, which can be understood as the shear and pressure drag forces exerted by the introduced elements on the flow. This forcing term is computed as the residuum between the total U_b and the other four componential contributions.

Table 2 provides a detailed decomposition of the bulk mean velocity U_b to identify the physical origins of the drag penalties associated with each stent configuration. In the laminar regime ($\mathrm{Re}_\tau = 60$), the observed drag increase is primarily driven by the structural forcing term U_b^D, which represents the additional viscous and pressure drag exerted by the ridges and scales with geometric complexity. Upon transitioning to the turbulent regime ($\mathrm{Re}_\tau = 180$), the random Reynolds shear stress U_b^{RS} becomes the dominant drag contributor across all geometries. The impact of SC is captured by the dispersive stress term U_b^{DS}, which is most pronounced for the straight-ridge (S1) and ambihelical (S3) configurations. Interestingly, U_b^{DS} remains negligible for the helical case (S2), suggesting that its SC behaves as a global cross-sectional rotation rather than localized dispersive vortices. For the ambihelical configuration S3, the combination of high Reynolds stress penalties and substantial structural forcing results in the highest overall drag, highlighting the severe cost of the intersections and complex ridge arrangement.

Table 2. Composition of the bulk mean velocity.

case	Re_τ	U_b/U_b^L	U_b^L/U_b^L	U_b^R/U_b^L	U_b^{RS}/U_b^L	U_b^{DS}/U_b^L	U_b^D/U_b^L
S0	60	1.00	1	0.00	0.00	0.00	0.00
	180	0.33	1	0.00	-0.68	-0.01	0.04
S1	60	0.99	1	0.01	0.00	0.00	-0.02
	180	0.34	1	0.01	-0.46	-0.23	0.01
S2	60	0.91	1	0.01	0.00	0.00	-0.10
	180	0.24	1	0.01	-0.68	0.00	-0.09
S3	60	0.85	1	0.02	0.00	-0.03	-0.14
	180	0.18	1	0.02	-0.61	-0.10	-0.12

Balance of Mean Vorticity

The balance of mean vorticity can be derived in general tensor notation (Aris 1989). The vorticity tensor is given by

$$\omega^i = \varepsilon^{ijk} g_{mj} u^m{}_{;k} \tag{6}$$

where ε is the Levi-Civita tensor, g_{ij} and g^{ij} are the contravariant and covariant metric tensors, respectively, u^m the (contravariant) velocity tensor and a subscript $_{;k}$ denotes the covariant derivative. Summation over repeated covariant-contravariant index pairs is implied. The mean vorticity balance for $\rho = \text{const.}$ then follows in flat space as

$$\begin{aligned} \rho \frac{\partial \langle \omega^i \rangle}{\partial t} + \rho \underbrace{\langle u^l \rangle \langle \omega^i \rangle_{;l}}_{\text{MC}} - \rho \underbrace{\langle u^i \rangle_{;l} \langle \omega^l \rangle}_{\text{VS}} \\ = \mu \underbrace{g^{jk} \langle \omega^i \rangle_{;jk}}_{\text{MD}} - \rho \underbrace{\varepsilon^{ijk} g_{mj} \langle u'^l u'^m \rangle_{;lk}}_{\text{TD}} \end{aligned} \tag{7}$$

While the left hand side represents the transport of ω by the Mean Convection (MC) and a Vortex Stretching (VS) term, the terms on the right hand side correspond to Molecular Diffusion (MD) and Turbulent Diffusion (TD). The physical components of the equation are obtained after multiplication with $h_i = \sqrt{g_{ii}}$.

In cylindrical coordinates, the physical components of the vorticity are given by

$$h_i \omega^i = \begin{pmatrix} \frac{1}{r}\frac{\partial u_z}{\partial \varphi} - \frac{\partial u_\varphi}{\partial z} \\ \frac{\partial u_r}{\partial z} - \frac{\partial u_z}{\partial r} \\ \frac{1}{r}\frac{\partial r u_\varphi}{\partial r} - \frac{1}{r}\frac{\partial u_r}{\partial \varphi} \end{pmatrix} \tag{8}$$

In components, eq. (7) becomes (compare with cartesian coordinates as given by Longo et al. (1998))

$$\text{MC} = \langle u_r \rangle \frac{\partial \langle \omega_z \rangle}{\partial r} + \frac{\langle u_\varphi \rangle}{r} \frac{\partial \langle \omega_z \rangle}{\partial \varphi} + \langle u_z \rangle \frac{\partial \langle \omega_z \rangle}{\partial z} \tag{9a}$$

$$\text{VS} = \langle \omega_r \rangle \frac{\partial \langle u_z \rangle}{\partial r} + \frac{\langle \omega_\varphi \rangle}{r} \frac{\partial \langle u_z \rangle}{\partial \varphi} + \langle \omega_z \rangle \frac{\partial \langle u_z \rangle}{\partial z} \tag{9b}$$

$$\text{MD} = \frac{1}{r}\frac{\partial}{\partial r}\left(r \frac{\partial \langle \omega_z \rangle}{\partial r} \right) + \frac{1}{r^2} \frac{\partial^2 \langle \omega_z \rangle}{\partial \varphi^2} + \frac{\partial^2 \langle \omega_z \rangle}{\partial z^2} \tag{9c}$$

$$\begin{aligned} \text{TD} = & -\frac{1}{r^3}\frac{\partial}{\partial r}\left(r^3 \frac{\partial \langle u'_r u'_\varphi \rangle}{\partial r} \right) + \frac{1}{r^2} \frac{\partial^2 \langle u'_r u'_\varphi \rangle}{\partial \varphi^2} \\ & + \frac{1}{r^2}\frac{\partial}{\partial \varphi}\frac{\partial}{\partial r}\left(r\left[\langle u'^2_r \rangle - \langle u'^2_\varphi \rangle \right] \right) \\ & - \frac{1}{r}\frac{\partial}{\partial z}\left(\frac{\partial r \langle u'_\varphi u'_z \rangle}{\partial r} - \frac{\partial \langle u'_r u'_z \rangle}{\partial \varphi} \right) \end{aligned} \tag{9d}$$

The vortex stretching and turbulent diffusion terms act as two different source / sink mechanisms for the axial vorticity, which Bradshaw (1987) characterises as 'skew-induced' generation – that is, deflection of existing mean vorticity – and 'stress-induced' generation by the (z component of the) curl of Reynolds stress divergence.

To elucidate the formation mechanism, the terms of eq. (9) for the tree considered geometries are displayed in fig. 4. Depending on the geometry and flow regime, different terms vanish; in particular the vortex stretching term vanishes identically for S1 (compare eq. (8) and eq. (9b) with $\partial \cdot / \partial z \equiv 0$), and the turbulent diffusion term is zero for laminar flow. For S1 at $\mathrm{Re}_\tau = 60$, u_z is the only velocity component and hence all terms of eq. (9) are zero. The turbulent S1 case thus clearly features stress-induced secondary flow, while the laminar S2 case can be described as skew-induced. For the turbulent S2 case, the axial vorticity is forced by both mechanisms; vortex stretching dominates turbulent diffusion almost everywhere. Consequently, mean convection is mostly driven and balanced by turbulent diffusion for the turbulent S1 case, and by vortex stretching for the turbulent S2 case. For S3 at $z = 0$, the observations align with those of S2 – turbulent diffusion being dominated by vortex stretching. Together with the comparably large magnitude of the in-plane components (see fig. 3), this indicates that the turbulent S3 case also features skew-induced secondary flow.

SUMMARY AND OUTLOOK

We carry out DNS to explore the effects of stent-like geometries with straight, helical, and ambihelical ridges with semi-circular cross-sections on the drag of the flow in both laminar ($\mathrm{Re}_\tau = 60$) and turbulent ($\mathrm{Re}_\tau = 180$) regimes. The numerical results demonstrate good agreement with experimental data, revealing that geometric complexity fundamentally alters the flow physics depending on the flow regime.

Under laminar conditions for all structured geometries, the presence of the ridges results in only weak modifications to the mean velocity profile. The induced pressure-driven motions of Prandtl's first kind are relatively weak, and the increase in the skin friction coefficient is modest. The bulk velocity decomposition indicates that in the laminar case, the drag penalty is primarily driven by increased structural drag, representing the additional viscous and pressure drag exerted by the ridges themselves. Conversely, in the turbulent regime, the skin friction coefficient increases significantly, particularly for the helical and ambihelical configurations. Upon transitioning to this turbulent state, the random Reynolds shear stresses become the dominant drag contributor across all geometries, accompanied by the formation of strong secondary motions. The topology and generation mechanisms of these turbulent secondary currents vary notably by geometric configuration. Straight ridges generate classical counter-rotating vortices of Prandtl's second kind; analysis of the mean vorticity balance confirms this motion is purely stress-induced, with turbulent diffusion balancing mean convection. In contrast, helical ridges induce a strong, global cross-sectional rotation. While this secondary flow is forced by a combination of pressure gradients and turbulence anisotropy in the turbulent regime, the vorticity balance reveals that vortex stretching significantly dominates turbulent diffusion, characterizing the motion as predominantly skew-induced, corresponding to motions of Prandtl's first kind. Meanwhile, the ambihelical ridges create a highly complex, three-dimensional flow more closely resembling flow over a fully rough surface.

The bulk mean velocity decomposition further highlights these topological differences. Dispersive stresses, which are directly linked to the presence of localized secondary currents, create significant drag penalties for the straight and ambihelical configurations. However, these dispersive stresses remain negligible for the helical case, confirming that its secondary motion functions as a uniform global cross-sectional rotation rather than localized, drag-inducing vortices. Ultimately, the ambihelical geometry represents the most severe case, as the combination of high Reynolds stress penalties and substantial structural forcing results in the highest overall drag.

Future work will focus on deeper flow analyses to elucidate the physical mechanisms driving the distinct skin friction trends observed in the turbulent regime for both the he-

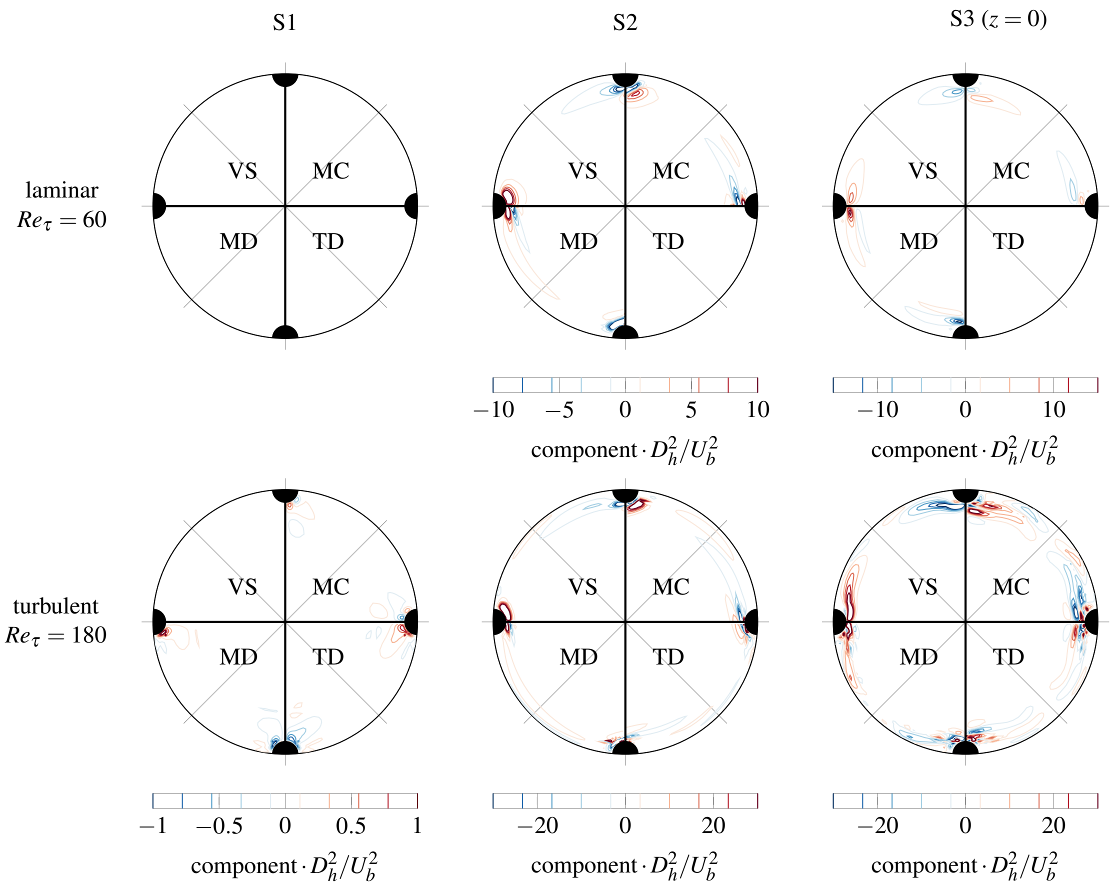

Figure 4. Terms of the vorticity balance eq. (9). Top row: $\mathrm{Re}_\tau = 60$, bottom row: $\mathrm{Re}_\tau = 180$; left column: S1, centre column: S2, right column: S3 at $z = 0$. Each quadrant of each subplot contains a different component: mean convection (first quadrant), vortex stretching (2$^{\mathrm{nd}}$), molecular diffusion (3$^{\mathrm{rd}}$) and turbulent diffusion (4$^{\mathrm{th}}$).

lical and ambihelical geometries. Additionally, the complex interplay between pressure-driven and turbulence-induced secondary motions (Prandtl's first and second kinds) requires further investigation. Upcoming studies will address this by systematically varying the ridge inclination angle relative to the streamwise axis to isolate and quantify these competing generation mechanisms.

ACKNOWLEDGEMENTS

A.Z. acknowledges the support of the European Union's Horizon Europe 2022 programme under the Marie Skłodowska-Curie grant agreement No. 101107322 (CARE), as well as the 2023 STARS Grants@UniPd programme. The authors acknowledge support by the state of Baden-Württemberg through bwHPC.

REFERENCES

Aris, R. 1989. *Vectors, Tensors, and the Basic Equations of Fluid Mechanics*. 2nd ed. Dover Books on Mathematics. New York: Dover Publications.

Benschop, H. et al. 2017. Drag reduction by herringbone riblet texture in direct numerical simulations of turbulent channel flow. *J. Turbul.* **18.8**, pp. 717–759.

Bradshaw, P. 1987. Turbulent Secondary Flows. *Annual Review of Fluid Mechanics* **19.1**, pp. 53–74.

Faisst, H. et al. 2004. Sensitive Dependence on Initial Conditions in Transition to Turbulence in Pipe Flow. *Journal of Fluid Mechanics* **504**, pp. 343–352.

Fischer, P. et al. 2022. NekRS, a GPU-accelerated spectral element Navier–Stokes solver. en. *Parallel Computing* **114**. Publisher: Elsevier BV, p. 102982.

Longo, J. et al. 1998. Solid/Free-Surface Juncture Boundary Layer and Wake. *Experiments in Fluids* **25.4**, pp. 283–297.

Marusic, I. et al. 2007. Laminar and turbulent comparisons for channel flow and flow control. *J. Fluid Mech.* **570**, pp. 467–477.

Mittal, K. et al. 2019. Nonconforming Schwarz-spectral element methods for incompressible flow. en. *Computers & Fluids* **191**, p. 104237.

Timmis, A. et al. 2024. European society of cardiology: the 2023 atlas of cardiovascular disease statistics. *European Heart Journal* **45.38**, pp. 4019–4062.

Vanderwel, C. et al. 2015. Effects of spanwise spacing on large-scale secondary flows in rough-wall turbulent boundary layers. *Journal of Fluid Mechanics* **774**, R2.